

Shock Temperatures in Calcite at 115 to 185 GPa

Stanley G. Love\* and Thomas J. Ahrens

Seismological Laboratory 252-21, California Institute of Technology, Pasadena, CA 91125

\* to whom correspondence should be directed. Current address:

Mail Stop 306-438, Jet Propulsion Laboratory, 4800 Oak Grove Drive, Pasadena, CA 91109.

Phone: (818) 354-9084 Fax: (818) 393-4773 E-mail: Stanley.G.Love@jpl.nasa.gov

prepared 26 January, 1998 for submission to *Earth and Planetary Science Letters*

18 pages 7 Figures 1 Table 5600 words

## ABSTRACT

We present optical pyrometer measurements of shock temperatures in crystalline calcite ( $\text{CaCO}_3$ ) which constrain its behavior in shock waves with amplitudes of 115 to 185 GPa. Experimental shocks were raised in calcite samples by impacts of tantalum plate projectiles accelerated to  $\sim 6$  km/s in a two-stage light gas gun. The shock waves were observed with a pyrometer recording radiant intensities in six optical and near-infrared wavebands. Shock temperatures were determined by fitting the pyrometer records to Planck grey-body functions. The resulting temperatures---3300K to 5400K across the pressure range studied---are significantly lower than predicted for the high-pressure phase of calcite, suggesting that one or more additional endothermic phase transitions take place. Two candidate phase transitions are decomposition to  $\text{CO}_2 + \text{CaO}$  (previously inferred to begin at  $\sim 50$  GPa) and melting (thought to begin at  $\sim 80$  GPa). Melting alone cannot explain the observed temperatures, which support model calculations assuming decomposition occurs. The present results are inconsistent with recent suggestions that the carbonate veins in martian meteorite Allan Hills 84001 are impact melt formed at  $\sim 50$  GPa. Two of our experiments employed imaging equipment in addition to the pyrometer. The imaging results show inhomogeneous intensity across the sample, consistent with previous inferences of localized melting and decomposition.

## INTRODUCTION

Shock waves can decompose carbonates such as calcite ( $\text{CaCO}_3$ ), releasing carbon dioxide ( $\text{CO}_2$ ) [Lange and Ahrens 1986]. This effect is more than a laboratory curiosity. The abundance of carbonate rocks on Earth raises the possibility that shocks from large meteorite impacts might liberate enough  $\text{CO}_2$  to warm the global climate via the greenhouse effect, an idea which has been examined as a potential killing mechanism in the great extinction at the end of the Mesozoic [Yang 1996, O'Keefe and Ahrens 1989]. In that particular case, greenhouse warming may have followed temporary (1--10 year) global cooling from stratospheric sulfate aerosols attributable to gypsum ( $\text{CaSO}_4 \cdot 2\text{H}_2\text{O}$ ) and anhydrite ( $\text{CaSO}_4$ ) at the Chicxulub impact site [Pope et al. 1994, Pope et al. 1997, Yang and Ahrens 1998]. Carbonates also occur on Mars [Soderblom 1992]. The atmosphere of Mars is much less massive than that of the Earth, and the martian climate might be proportionally more sensitive to impact-generated gases. Unfortunately, consensus on the mechanism and efficiency of shock decomposition in carbonates has remained elusive, frustrating efforts to describe the effects of large impacts on the climate history of both Earth and Mars. Better understanding of shock devolatilization would also improve models of the production and distribution of impact melt, which is depleted in impact target rocks rich in carbonates, sulfates, and hydrates [Kieffer and Simonds 1980, Greive and Cintala 1992, Pierazzo et al. 1997]. Furthermore, it has recently been proposed that the interesting carbonate veins in martian meteorite Allan Hills 84001 are impact melt [Scott et al. 1997]. This interpretation requires carbonates to resist dissociation under shock pressures and temperatures sufficient for melting, inconsistent with some experimental results [Yang 1996, Kondo and Ahrens 1983, Lange and Ahrens 1986].

To better understand shock decomposition of carbonates, Yang and Ahrens [Yang 1996, Yang and Ahrens 1998] used an interferometric velocity measurement technique (VISAR) to monitor the adiabatic expansion of porous  $\text{CaCO}_3$  (chalk) shock-compressed to pressures from 4 to 19 GPa. Their particle expansion velocity profiles indicated unexpectedly high values of entropy being generated in the shock. This result suggested that  $\text{CO}_2$  was produced during the shock

compression phase of their experiments, which was surprising for two reasons. First, the customary expression of thermodynamic equilibrium favors a solid phase ( $\text{CaCO}_3$ ) over a mixed solid-plus-gas phase ( $\text{CaO} + \text{CO}_2$ ) at high pressure; by this reasoning, decomposition should occur during release rather than compression. Second, the corresponding threshold pressure for complete decomposition of *crystal* calcite was inferred to be 103 GPa, higher than inferred by other researchers [O'Keefe and Ahrens 1989] using results from shock recovery experiments [Lange and Ahrens 1986]. The unanticipated character of the foregoing results justifies further investigation.

A good method for such an investigation is to measure shock temperatures, which have been used as a diagnostic to identify phase transitions and chemical reactions such as decomposition in past shock experiments [Nellis et al. 1991, Holland and Ahrens 1997]. The energy required to release  $\text{CO}_2$  from calcite corresponds to shock temperatures  $\sim 2500$  K lower than expected if no decomposition occurs [Yang 1996], a difference easily resolvable with optical pyrometry [Boslough and Ahrens 1989, Yang 1996]. Accordingly, we describe here a series of six optical pyrometer shock temperature experiments on calcite at shock pressures of 115 to 185 GPa, and relate the results to the predicted behavior of calcite under those conditions. We also discuss imaging experiments carried out in tandem with two of the temperature measurements. The imaging results help illuminate the physical processes leading to the temperatures measured in this work and in previous experiments on shocked calcite [Kondo and Ahrens, 1983].

## EXPERIMENTAL METHOD

We obtained optically flawless single-crystal calcite disks 12.7 mm in diameter by 3 mm thick from the Karl Lambrecht company. Each crystal's c-axis was oriented parallel to the polished circular face of the sample. In preparation for use in the experiment, each sample was carefully cleaned and then sputter-coated on one face with a layer of Ag metal approximately 1500 Å thick. Silver films of this thickness are opaque and emit little light when shocked; they are thus used in optical shock temperature experiments to suppress the "gap flash" observed when the driver plate

first strikes the sample, and to block radiation from the hot driver plate [Svendsen and Ahrens 1990, Holland and Ahrens 1997]. As shown in Fig. 1, the uncoated (downrange) side of the calcite sample faced toward the experimental optics. The uncoated side was partially covered by an opaque annular mask. The mask blocked emission from reverberating shocks near the edges of the sample which might otherwise have polluted the radiation from the geometrically simple main shock. The mask also decreased the total amount of light from the experiment to avoid saturating the optical pyrometer photodetectors.

The coated side of each calcite sample was mounted to a 0.5-mm-thick Ta "driver plate." The combined assembly was then mounted in the target chamber of the Lindhurst Laboratory 25-mm two-stage light gas gun. Shorting pins on the target holder faced uprange to sense the arrival of the Ta "flyer plate" (Fig. 1) and begin data recording for the experiment. The impact of the flyer plate---launched in a Lexan sabot at 5.0 to 6.9 km/s (Table 1)---upon the driver induced a shock in the latter which was transmitted in turn to the calcite sample. The hot, luminous shock propagated through the calcite sample in ~200 ns (the duration of the experiment).

The optical pyrometer layout is diagrammed in Fig. 2. Light from a shock passes through the hole in the mask and reflects at a sacrificial turning mirror downrange of the sample. (The mirror is destroyed when debris from the flyer, driver, and target reaches it, long after experimental data recording has ceased.) The turning mirror directs the light through a port in the side of the target chamber, where it passes through a neutral-density filter and focusing lenses into a bundle of optical fibers. The fiber bundle distributes light evenly to six wideband filters (center wavelengths 451.5, 555.5, 603.7, 661.5, 748.2, and 904.0 nm). Behind each optical filter lies a photodetector (New Focus, Inc. Model 1801) which converts the light intensity into a proportional electrical signal. The output of the detectors is recorded by 500 MHz and 1 GHz sample rate Gould Model 4074 and Hewlett-Packard Models 54111D and 54540A digital oscilloscopes. The pyrometer used in this work is based on previous generations of pyrometers [Lyzenga and Ahrens 1979, Boslough and Ahrens 1989] and described in detail by Yang [Yang 1996]. We calibrated the optical pyrometer before each shot with a NIST-certified 1000 W standard light source

(Optronic Laboratories Model OL200M, using an Optronic Laboratories Model 83A power supply) placed at the position later occupied by the sample, with the rest of the optical system in precisely the same configuration as in the experiment. The pyrometer is useful for measuring temperatures of ~3000 K and above. The upper limit of temperature is defined by the equation of state of the target material and the 7.3 km/s maximum muzzle velocity of the light gas gun. In the present study, the maximum measured temperature was near 5500 K.

Experiments 305 and 308 included imaging equipment as well as the optical pyrometer. For these trials, the turning mirror was replaced with a sacrificial 50% beamsplitter which reflected ~50% of the light from the experiment toward the optical pyrometer and passed the remaining ~50% to a second turning mirror, which directed the transmitted beam through a port in the wall of the target tank and thence to a camera (see Fig. 2). Experiment 305 employed a Cordin 160 streak camera with a TRW Model 5b streak unit and Kodak T-Max 400 film. The camera imaged a slit placed across the center of the sample mask image. The slit image was swept across the film in a direction perpendicular to the slit's long axis during a 1.6  $\mu$ s interval that included the ~200-ns-long shock-induced light pulse from the target. The resulting photograph (Fig. 6) shows one dimension of spatial information (along the slit) and one dimension of time variability (perpendicular to the slit). Experiment 308 used the same camera and film, but employed a Cordin 1643 framing unit to produce three two-dimensional images (Fig. 7) of the entire visible target face during the experiment. Each exposure lasted 20 ns; the interframe delay was 50 ns. Simultaneous pyrometry and imaging is a new capability for our laboratory.

## RESULTS

Table 1 summarizes the conditions and results of each experiment. The shock pressures shown in the table are calculated impedance match solutions using linear shock particle-velocity equation of state (EOS) parameters for Ta ( $\rho_0 = 16,649 \text{ kg m}^{-3}$ ,  $C_0 = 3.31 \text{ km s}^{-1}$ ,  $S = 1.306$ ) and for the high-pressure phase (hpp,  $> \sim 14 \text{ GPa}$  [Yang 1996]) of calcite ( $\rho_0 = 3,100 \text{ kg m}^{-3}$ ,  $C_0 = 5.58$

km s<sup>-1</sup>,  $S = 1.25$ ) [Ahrens and Johnson 1995]. The EOS parameters are also used to predict the time required for the shock to propagate through the sample, which aids in identifying the relevant part of the data record in case of timing uncertainties.

Light from the shocked target is recorded on each of the pyrometer's six channels, producing traces like that of Fig. 3. In the most easily interpreted experiments [Boslough 1985], the pyrometer output is a square wave indicating constant temperature and emissivity as the shock wave traverses the sample. The present results are more difficult to characterize. The prominent initial "gap flash" in Fig. 3 varies from shot to shot; in some cases it is not seen. We attribute the flash to discontinuities between the target and driver plate and to imperfections in the flash-suppressant Ag coating. After the initial flash, the signal remains level for much of the experiment. This "plateau" value (indicated by the upper dashed horizontal line in Fig. 3) is maintained for a different duration in each shot; some subjective judgment is required to quantify it (see below for a discussion of the uncertainty thereby introduced). The plateau value is used to find the radiant intensity in each waveband as described below. Toward the end of the experiment, the signal again increases. We interpret this late-time brightening as emission from the lateral sides of the sample scattered into the unmasked region viewed by the pyrometer, and from "hot spots" discussed below. Boslough [Boslough 1985] attributes pyrometer profiles with shapes like that of Fig. 3 to absorption within the sample which decreases as the shock approaches the rear surface. That model, however, predicts variation in emissivity but not in temperature for colorless samples like those used here; calculations of the temperature and emissivity as a function of time [K. Holland, personal communication] indicate increases in both. The Boslough mechanism also cannot explain signal growth of a factor of two or more (as seen in some of our trials) in samples whose total measured absorbance at optical wavelengths is less than five percent. We propose an alternate explanation. As the shock wave propagates through the sample, the radiation it induces is not perfectly uniform ([Kondo and Ahrens 1983]; see also imaging results below). During the experiment, the emitted light includes a contribution from anomalous "hot spots" with locally higher temperature. The hot spots grow in number (and thus in area, corresponding to increasing

emissivity and to rising temperature averaged over the sample's visible face) as the shock proceeds through the sample. This behavior is best seen in Fig. 6, the streak record of Experiment 305.

To find a shock temperature, we find the plateau voltage level for each of the pyrometer's six channels. Each voltage level is then compared to that produced when the standard lamp (discussed above) is placed at the target location during calibration. Within the linear range of the photodetectors (up to 1.0 V), the voltage is directly proportional to the intensity. Relating the background-subtracted experimental and calibration voltages to one another and scaling to the known spectral irradiance of the calibration lamp yields the experimental light intensity in each pyrometer channel. The six resulting intensity values are then used to find a best-fit Planck spectral irradiance curve with a specific temperature and emissivity. Figure 4 illustrates the pyrometer intensity values (with uncertainties estimated from the reproducibility of judging the "plateau" values) and resulting best-fit Planck curve and its corresponding temperature and emissivity for a typical shot (Experiment 305). Table 1 gives the best fit temperatures and emissivities for all six experiments. The temperatures are plotted as a function of shock pressure in Fig. 5.

Several effects contribute to the uncertainties in temperature and emissivity. The first is the character of the radiation itself: it is not a perfect grey-body (that is, a thermal radiator with non-unit emissivity and no emission lines). Kondo and Ahrens [Kondo and Ahrens 1983] noted a small contribution from line emission in the spectral profile of shocked calcite at 40 GPa, but the reported emission perturbs rather than dominates the underlying continuum. Furthermore, if the radiant intensity of shocked calcite varied strongly from the grey-body model, the chi-square per degree freedom parameters for the fitted curves would exceed the typical values of 1 to 2 found here. The imaging experiments described below clearly show nonuniform distribution of light across the face of the sample, but this nonuniformity will simply appear as altered emissivity in the present calculations. Thus, departure from pure grey-body radiation is not expected to be a major source of error. Because of the care with which the standard calibration lamp is installed, operated, and itself calibrated, we do not consider the conversion of voltage to intensity using the



standard lamp to be a significant source of error. Similarly, the finite bandpass of the optical filters may contribute some uncertainty, but any such effect is minimized by using the same filters for both calibration and experiment.

A larger source of uncertainty in the present results is the reproducibility of estimating the plateau and background voltage values. For most experiments, we used three independent assessments of each plateau to quantify these uncertainties (usually 3 - 5 %), which were used in turn to derive error estimates for the six intensity values used in Planck curve fitting. (In cases where a channel's output signal approached the 1.0 V linear limit for the photodetectors, we increased the estimated uncertainty to lower that channel's statistical weight in the fit. If the signal exceeded 1.0 V, we disregarded data from that channel altogether.) The most significant errors arise in fitting Planck curves to the data points. Because of the finite uncertainty in each point, a range of temperatures and emissivities fit the data indistinguishably well. Boslough and Ahrens [Boslough and Ahrens 1989] estimate that the uncertainty in temperature from this effect is about 5%, and that the uncertainty in emissivity is as much as 50%. Both of these values dominate the other sources of error discussed here, and should be considered the best estimate of uncertainty for the temperatures and emissivities we report. Our emissivity results in particular (see Table 1) seem to corroborate the estimate of Boslough and Ahrens [Boslough and Ahrens 1989]: several are greater than unity, which is physically impossible for a blackbody. Our mean emissivity and its standard deviation are  $0.98 \pm 0.37$ ; this 38% uncertainty is consistent with the 50% estimate. Note that our highest emissivity value (1.6) would demand a temperature increase of 12% to bring it down to a physically plausible value of 1.0 with the same total light output. Thus, 12% should be taken as an upper limit to the uncertainty for the temperatures we present. We conservatively show 10% uncertainty for most of the points in Fig 5; a larger uncertainty is assumed for Experiment 298, which had fewer channels of useful data. The meaning of the temperature and emissivity values and their uncertainties will be discussed below.

We now describe the results of the imaging experiments carried out in tandem with the temperature measurements of Experiments 305 and 308. In Experiment 305, the camera was in

streak mode (Fig. 6). The slit image was swept across film during the experiment, providing a time-resolved record (in the vertical direction) of the horizontal slit. The gap flash (bright line) at the bottom marks the beginning of the experiment. Moving upward reveals the slit as its image changed during the experiment. About 200 ns after the shock enters the sample, the entire slit brightens dramatically, marking the shock wave's arrival at the sample's rear free surface. The important result is that the sample's visible face contains bright spots that appear, disappear, and exhibit dramatic apparent lateral motion (note the slanted bright line in the record) during the experiment. In general, the number and area of bright spots increases with time. This behavior verifies our interpretation of the signal growth noted above and justifies our use of the plateau voltages (which occur early in the experiment, while pollution by anomalous bright spots is minimal) in calculating shock temperatures.

In framing mode (Experiment 308, Fig. 7), the camera images the unmasked central portion of the sample (5 mm in diameter) three times. Figure 7 shows the outcome, unfortunately cluttered with stray light from the camera image intensifier tube. The three circular spots are the sample images. The brightest (uppermost) one corresponds to the increase in intensity at the end of the experiment. The bright spot in the first (bottommost) is probably a bright point in the shock analogous to those seen in Experiment 305, although it could also be a hole in the Ag flash-suppressant coating. The former interpretation is consistent with the inhomogeneous radiation seen in Experiment 305 and with the results of Kondo and Ahrens [Kondo and Ahrens 1983].

## DISCUSSION

### Shock Temperatures

Figure 5 shows the shock temperatures from this study, plotted alongside theoretical values calculated for shock-induced breakdown of  $\text{CaCO}_3$  to  $\text{CaO}$  and  $\text{CO}_2$  beginning at  $\sim 50$  GPa and reaching completion at  $\sim 105$  GPa [Yang 1996; Yang and Ahrens 1998]. Analogous values for intact calcite [Yang 1996; Yang and Ahrens 1998; W. Anderson, private communication] are also

shown. The calculations for intact calcite presume the following parameters for the high pressure phase (hpp) of calcite: Standard Temperature and Pressure (STP) density =  $3100 \text{ kg m}^{-3}$ ;  $K_{so} = 96.5 \text{ GPa}$ ;  $dK_s/dP=4.0$ ,  $\Gamma = 1.183\sqrt{V/V_0}$ , where  $V$  and  $V_0$  are the high-pressure and STP specific volumes respectively; initial sample density =  $2712 \text{ kg m}^{-3}$ , STP energy of transition to hpp =  $0.02 \text{ MJ/kg}$ ,  $C_v = 1246 \text{ J/kg}\cdot\text{K}$ .

The experimental temperatures fall near the melting line of Kerley [1989] to  $\sim 140 \text{ GPa}$ . They also lie close to the calcite decomposition (breakdown) curve at higher pressures. Because the energy required for breakdown is so much larger than the heat of fusion [e.g., Yang 1986], melting alone cannot explain the low temperatures observed here. The present results thus strongly support the breakdown hypothesis, and do not illuminate the question of melting. Uncertainties in the experiments, phase relations, and calculated shock decomposition temperatures prevent us from drawing any stronger conclusions.

The present results conflict with the recent proposition that the interesting carbonate structures in martian meteorite ALH84001 were emplaced as impact melt in a shock with a pressure near  $50 \text{ GPa}$  [Scott et al. 1997]. The pressure is estimated from other shock features identified in the rock. We present two lines of reasoning in support of this conclusion.

The first argument is based on the agreement of our findings with previous work [Yang 1996, Lange and Ahrens 1986] showing that calcite begins decomposing at  $\sim 50 \text{ GPa}$  and decomposes completely at  $\sim 105 \text{ GPa}$ . Shock temperatures calculated assuming such decomposition (dashed line in Fig. 5) first enter the melt field of the phase diagram [Kerley 1989] at  $140 \text{ GPa}$ . Because the pressure of incipient melting is significantly higher than the  $\sim 105 \text{ GPa}$  at which calcite fully decomposes to  $\text{CO}_2 + \text{CaO}$ , the breakdown model suggests that intact, impact-melted calcite is not possible at all, and that the calcite in the Allan Hills meteorite cannot be impact melt.

A second (and stronger) argument is independent of the breakdown model. Regardless of whether calcite decomposes at the pressures investigated here, the experimental shock temperatures (plotted in Fig. 5) define a trend that enters the melt field at shock pressures of  $130\text{-}170 \text{ GPa}$ .

Such high pressures are firmly excluded by the textural evidence used to constrain the shock history of ALH 84001 [Scott et al. 1997]. Taken together, these arguments suggest that impact melting of calcite cannot occur at  $\sim 50$  GPa (and indeed may require pressures several times higher), and furthermore that calcite may never endure shocks strong enough to cause melting without decomposing first. We thus conclude that the ALH 84001 carbonates cannot be impact melt emplaced at  $\sim 50$  GPa.

### Inhomogeneous Shock Radiation

Kondo and Ahrens [Kondo and Ahrens 1983] studied calcite shocked at pressures up to 40 GPa and reported extremely high temperatures and very low emissivities (nearly 3 times the calculated value and  $\sim 0.0025$  respectively; see Fig. 5), indicative of inhomogeneous emission of radiation possibly attributable to shear banding analogous to that observed in shocked crystalline quartz [Brannon et al. 1983]. Shear banding in calcite is noted at pressures below  $\sim 40$  GPa [Kondo and Ahrens 1983], and is usually characterized by visible emission appearing only along crystallographically controlled planes in the sample. The pressure regime of the present experiments, is much higher than the range where shear banding has been noted [Brannon et al. 1983]. We nonetheless see evidence for inhomogeneous emission. As discussed above, signal growth during the experiment (Fig. 3) indirectly indicates inhomogeneity, while the imaging experiments (Figs. 6 and 7) show it directly.

The temperatures and emissivities we find are near the expected range and near unity respectively, inconsistent with the findings of Kondo and Ahrens [Kondo and Ahrens 1983]. Instead, we find a generally bright, opaque shock front with a few localized bright spots. These results, combined with the higher pressure regime, lead us to the conclusion that the effect we observe is not shear banding. An interesting possibility, however, is that the irregularities we note could be localized concentrations of shock energy "seeded" by local shear band instabilities during the initial shock pressure increase. In this scenario, shear slippage produces local temperature increases up to the melting or vaporization point, where the material loses all strength and heat

input through frictional sliding ceases. This interpretation meshes well with the notion that the low shock temperatures observed here are caused by partial to complete decomposition and possibly also melting.

## SUMMARY AND CONCLUSIONS

We measured shock temperatures at 115 to 185 GPa in calcite using an optical pyrometer. The temperatures we obtain are significantly lower than predicted for simple compression of calcite. They are consistent with decomposition of calcite into CaO and CO<sub>2</sub> during shock compression, as proposed by Yang [Yang 1996, Yang and Ahrens 1998]. They are also consistent with melting. If calcite decomposes, our results support Yang's estimate of the amount of CO<sub>2</sub> released in the formation of the Cretaceous/Tertiary impact event [Yang 1996], corroborate the assertion that volatiles released from the target rock under peak shock loading can diminish and disperse crater impact melt [Kieffer and Simonds 1980, Greive and Cintala 1992, Pierazzo et al. 1997], and suggest that calcium carbonate cannot be liquefied under shock pressures below ~ 140 GPa without first decomposing. Local melting or decomposition seeded by local shear band instabilities [Brannon et al. 1983] is also consistent with the spotty emission of radiation indicated by our time-dependent intensity profiles and imaging results.

These experiments have yielded interesting insights into the behavior of calcite at high shock pressures, but much more work remains to be done. Of greatest interest are further shock recovery experiments, VISAR work, and theoretical calculations to better understand the shock decomposition of calcite. Shock temperature work at somewhat lower pressures (perhaps using pyrometry at wavelengths longer than 1  $\mu\text{m}$ ) might also provide important further constraints on the behavior of calcite in the calculated regimes of incipient melting or decomposition.

## ACKNOWLEDGMENTS

We thank Kathleen Holland, Mike Long, Papo Gelle, and Alberto DeVora for technical assistance with this work. This research was supported by NASA. This paper is Contribution 8498 of the Division of Geological and Planetary Sciences.

## REFERENCES

- [Lange and Ahrens 1986] M. A. Lange and T. J. Ahrens, Shock-induced CO<sub>2</sub> loss from CaCO<sub>3</sub>: Implications for early planetary atmospheres, *Earth Planet. Sci. Lett.* **77**, 409-418, 1986.
- [Yang 1996] W. Yang, Impact volatilization of calcite and anhydrite and the effect on global climate from K/T impact crater at Chicxulub, 143 pp., Ph.D. Dissertation, California Institute of Technology, 1996.
- [O'Keefe and Ahrens 1989] J. D. O'Keefe and T. J. Ahrens, Impact production of CO<sub>2</sub> by the Cretaceous-Tertiary extinction bolide and the resultant heating of the Earth, *Nature* **338**, 247-249, 1989.
- [Pope et al. 1994] K. O. Pope, K. H. Baines, A. C. Ocampo, and B. A. Ivanov, Biospheric effects of sulfuric acid particles produced by the Chicxulub Cretaceous/Tertiary impact, *Earth Planet. Sci. Lett.* **128**, 719-725, 1994.
- [Pope et al. 1997] K. O. Pope, K. H. Baines, A. C. Ocampo, and B. A. Ivanov, Energy, volatile production, and climatic effects of the Chicxulub Cretaceous/Tertiary impact, *J. Geophys. Res.* **102**, 21,645-21,6xx, 1997.
- [Yang and Ahrens 1998] W. Yang and T. J. Ahrens, Shock vaporization of anhydrite and global effects of the K/T bolide, *Earth Planet. Sci. Lett.*, submitted.
- [Pierazzo et al. 1997] E. Pierazzo, A. M. Vickery, and H. J. Melosh, A reevaluation of impact melt production, *Icarus* **127**, 408-423, 1997.
- [Grieve and Cintala 1992] R. A. F. Grieve and M. J. Cintala, An analysis of differential impact melt-crater scaling and implications for the terrestrial impact record. *Meteoritics* **27**, 526-538, 1992.
- [Kieffer and Simonds 1980] S. W. Kieffer and C. H. Simonds, The role of volatiles and lithology in the impact cratering process. *Rev. Geophys. Space Phys.* **18**, 143-181, 1980.
- [Kondo and Ahrens 1983] K. Kondo and T. J. Ahrens, Heterogeneous shock-induced thermal radiation in minerals, *Physics and Chemistry of Minerals* **9**, 173-181, 1983.

- [Holland and Ahrens 1997] K. G. Holland and T. J. Ahrens, Melting of (Mg,Fe)(2)SiO<sub>4</sub> at the core-mantle boundary of the earth, *Science* **275**, 1623-1625, 1997.
- [Nellis et al. 1991] W. J. Nellis, H. B. Radousky, D. C. Hamilton, A. C. Mitchell, and N. C. Holmes, Equation-of-state, shock-temperature, and electrical-conductivity data of dense fluid nitrogen in the region of the dissociative phase-transition, *J. Chem. Phys.* **94**, 2244-2257, 1991.
- [Lyzenga and Ahrens 1979] G. A. Lyzenga and T. J. Ahrens, Multiwavelength optical pyrometer for shock compression experiments, *Rev. Sci. Instruments* **50**, 1421-1424, 1979.
- [Boslough and Ahrens 1989] M. B. Boslough and T. J. Ahrens, A sensitive time-resolved radiation pyrometer for shock-temperature measurements above 1500 K, *Rev. Sci. Instruments* **60**, 3711-3716, 1989.
- [Svendsen and Ahrens 1990] B. Svendsen and T. J. Ahrens, Shock-induced temperatures of CaMgSi<sub>2</sub>O<sub>6</sub>, *J. Geophys. Res.* **95**, 6943-6953, 1990.
- [Ahrens and Johnson 1995] T. J. Ahrens and M. L. Johnson, Shock wave data for minerals, in Mineral Physics and Crystallography, A Handbook of Physical Constants, vol. 2, edited by T. J. Ahrens, pp. 143 - 183, Amer. Geophys. Union, Washington DC, 1995.
- [Scott et al. 1997] E. R. D. Scott, A. Yamaguchi, and A. N. Krot, Petrological evidence for shock melting of carbonates in the martian meteorite ALH84001, *Nature* **387**, 377-379, 1997.
- [Boslough 1985] M. B. Boslough, A model for time dependence in shock-induced thermal radiation of light, *J. Appl. Phys.* **58** (9), 3394-3399, 1985.
- [Soderblom 1992] L. A. Soderblom, The composition and mineralogy of the martian surface from spectroscopic observations: 0.3  $\mu$ m to 50  $\mu$ m, in: Mars, H.H. Kieffer, B. M. Jakosky, C. W. Snyder, and M. S. Matthews, eds., pp. 557-593, University of Arizona Press, Tucson, 1992.
- [Brannon et al. 1983] P. J. Brannon, C. Konrad, R. W. Morris, E. D. Jones, and J. R. Asay, Studies of the spectral and spatial characteristics of shock-induced luminescence from x-cut quartz, *J. Appl. Phys.* **54**, 6374-6381, 1983.



[Kerley 1989] G. I Kerley, Equations of state for calcite minerals. I. Theoretical model for dry calcium carbonate, *High Pressure Research* **2**, 29-47, 1989.

## FIGURE CAPTIONS

Figure 1. Cartoon of the lexan projectile with its tantalum flyer plate approaching the target assembly which includes the shorting pins, tantalum driver plate, and silver-coated sample with annular mask.

Figure 2. Cartoon of the experimental setup during an experiment. Light from the shock front escapes through the hole in the center of the mask on the downrange face of the sample. A sacrificial turning mirror directs the light through a window in the evacuated target tank, then into a bundle of optical fibers which distributes the light equally through six broadband optical filters (center wavelengths 451.5, 555.5, 603.7, 661.5, 748.2, and 904.0 nm). Behind each filter is a photodiode, amplifying electronics, and a high-speed digital oscilloscope which records the signal. In two experiments (305 and 308) the first turning mirror is replaced with a 50% beamsplitter which transmits half the light to a second turning mirror and thence via a window to a streak or framing camera.

Figure 3. Oscilloscope trace from a typical pyrometer channel (channel 3, 603.7 nm center wavelength, experiment 301). Note the strong “gap flash” attributable to discontinuities between the target and driver plates, and to imperfections in the silver flash-suppressant coating. The dashed line indicates the “plateau” used to calculate the shock temperature. The signal growth toward the end of the experiment is attributable to scattered light from shocked and released material on the sample lateral surfaces and to small increases in both the temperature and emissivity of the emitting region of the main shock.

Figure 4. Sample fit of pyrometer irradiances to a Planck grey-body function for a typical experiment (# 305). Error bars are estimated from uncertainty in the plateau value and from electronic noise.

Figure 5. Shock temperature of calcite plotted as a function of shock pressure. The values found in this work are shown with conservative uncertainties of  $\pm 10\%$  for most points (experiment 298 had fewer channels of useful data and a correspondingly larger uncertainty). Also plotted are calculated shock Hugoniot temperatures ([Yang 1996]; W.

Anderson, private communication) for crystal calcite with (dotted line) and without (solid line) decomposition. The data are more consistent with the former interpretation. Also shown is the datum of Kondo and Ahrens [Kondo and Ahrens 1983] with a very high shock temperature and very low emissivity (0.0025) interpreted as shear banding.

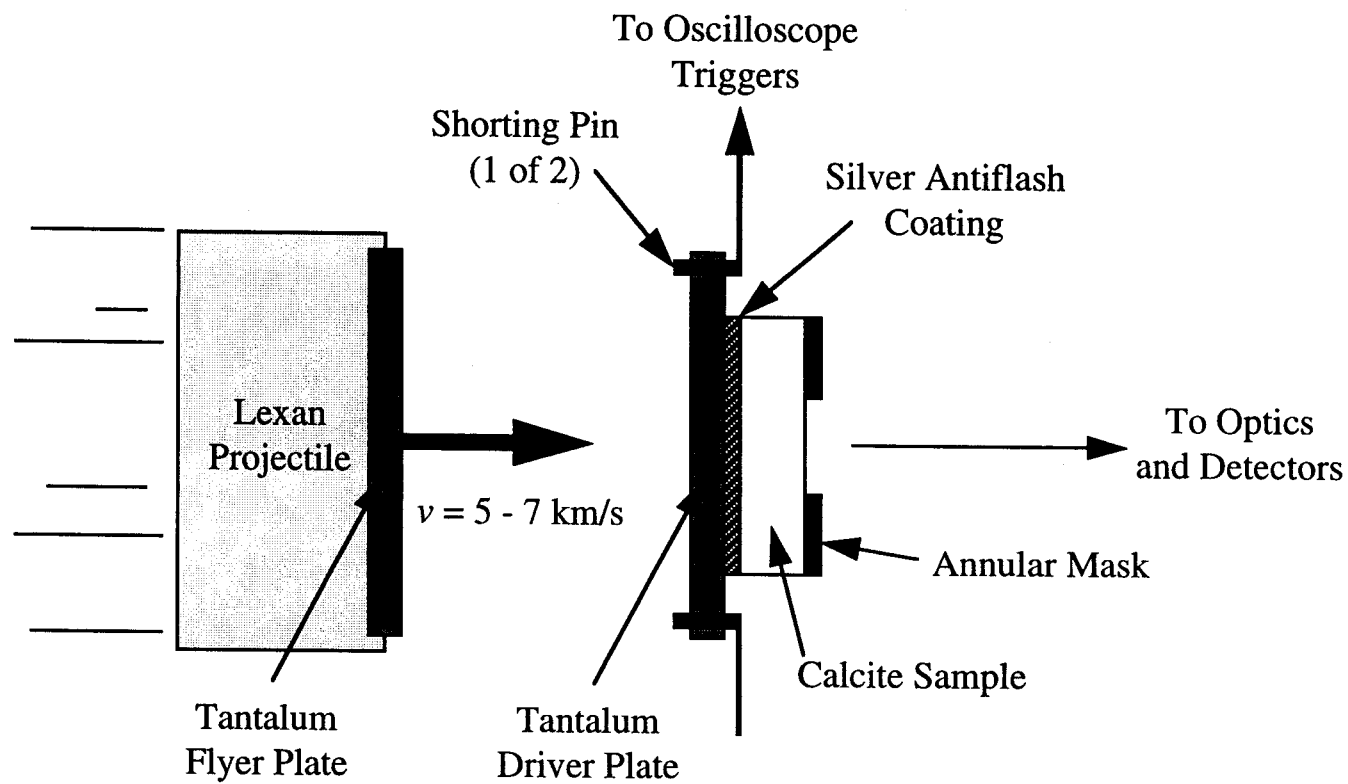
Figure 6. Streak camera image record of Experiment 305. Time progresses in the vertical direction. The bright line at the bottom of the photograph corresponds to the initial "gap flash" often seen when the shock enters the sample. The dark discontinuity near the top of the record indicates the shock wave's exit from the rear of the sample  $\sim 200$  ns later. The horizontal direction denotes position along the  $\sim 4$  mm long linear slit. Note the appearance and disappearance of bright areas along the slit. The bright line on the left of the streak record is not vertical, suggesting an anomalously hot region of the shock front with apparent rapid ( $\sim 2$ -3 mm/ $\mu$ s) lateral motion.

Figure 7. Framing camera images from Experiment 308. Each frame is exposed for 20 ns, with interframe delays of 50 ns. The photograph is unfortunately cluttered with stray light from the camera image intensifier tube. The three circular images, corresponding to the viewable sample rear surface (5-mm in diameter), are the data. The brightest (uppermost, #3) image corresponds to the increase in brightness immediately before the shock exits the sample free surface. The bright spot in the first image (bottommost, #1) is probably a bright point at the shock front analogous to those seen in Fig. 6.

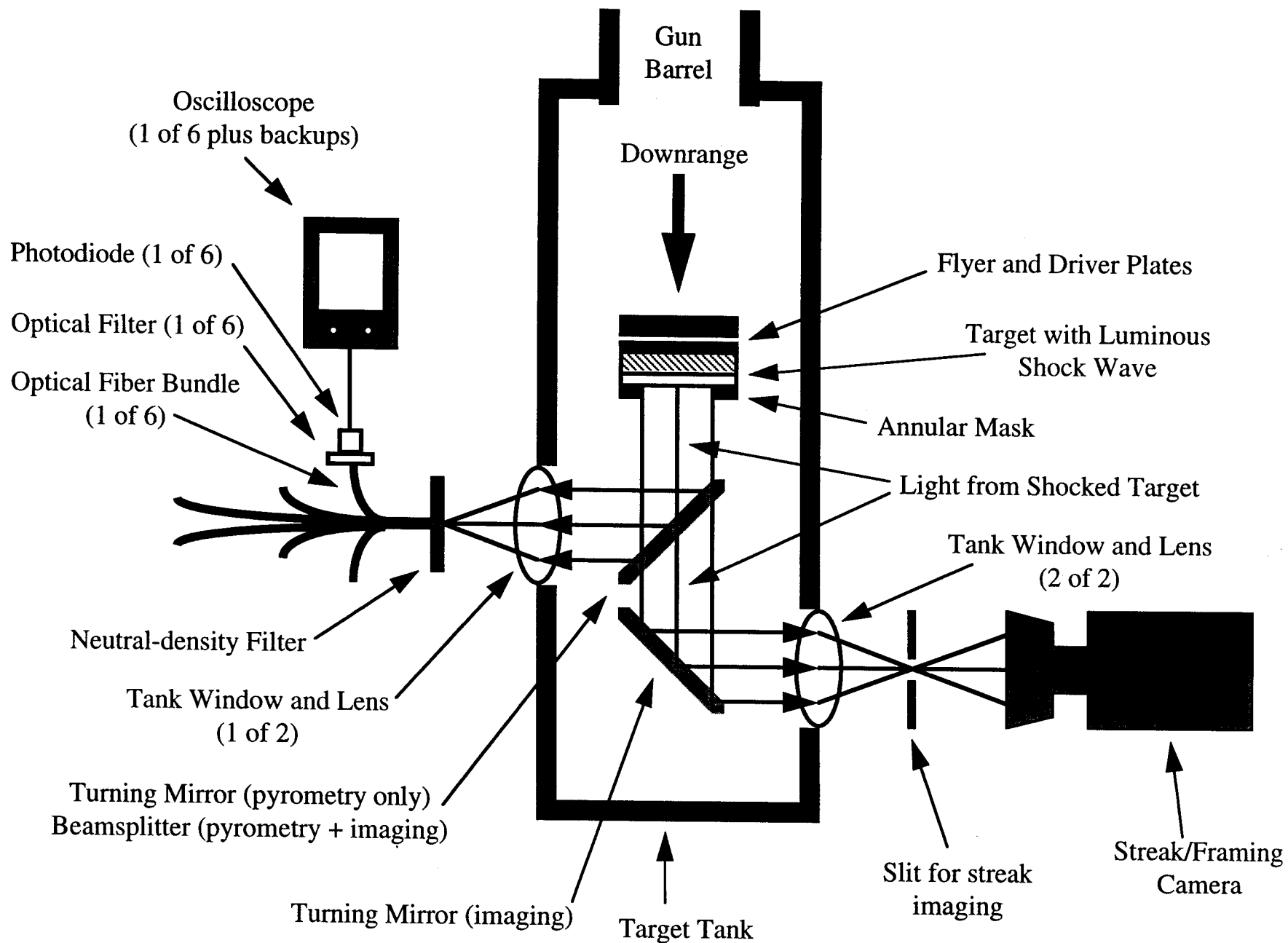
TABLE 1

Table 1. Experimental Conditions

Experiment #	Sample #	Projectile Velocity (km/s)	Pressure (GPa)	Fit Temperature (K)	Fit Emissivity	Fit $\chi^2$ per ° Freedom
299	2	6.93 $\pm$ 0.01	184.5 $\pm$ 1.0	5430 $\pm$ 540	0.55 $\pm$ 0.40	2.10
298	1	6.71 $\pm$ 0.01	175.8 $\pm$ 1.0	5040 $\pm$ 1000	1.10 $\pm$ 0.40	0.72
300	3	6.37 $\pm$ 0.01	162.7 $\pm$ 1.0	5425 $\pm$ 600	0.77 $\pm$ 0.40	1.00
301	5	6.00 $\pm$ 0.01	149.0 $\pm$ 1.0	4530 $\pm$ 450	1.60 $\pm$ 0.40	2.36
305	7	5.48 $\pm$ 0.01	130.6 $\pm$ 1.0	4410 $\pm$ 440	0.75 $\pm$ 0.40	3.71
308	6	5.00 $\pm$ 0.01	114.6 $\pm$ 1.0	3250 $\pm$ 400	1.15 $\pm$ 0.40	1.53

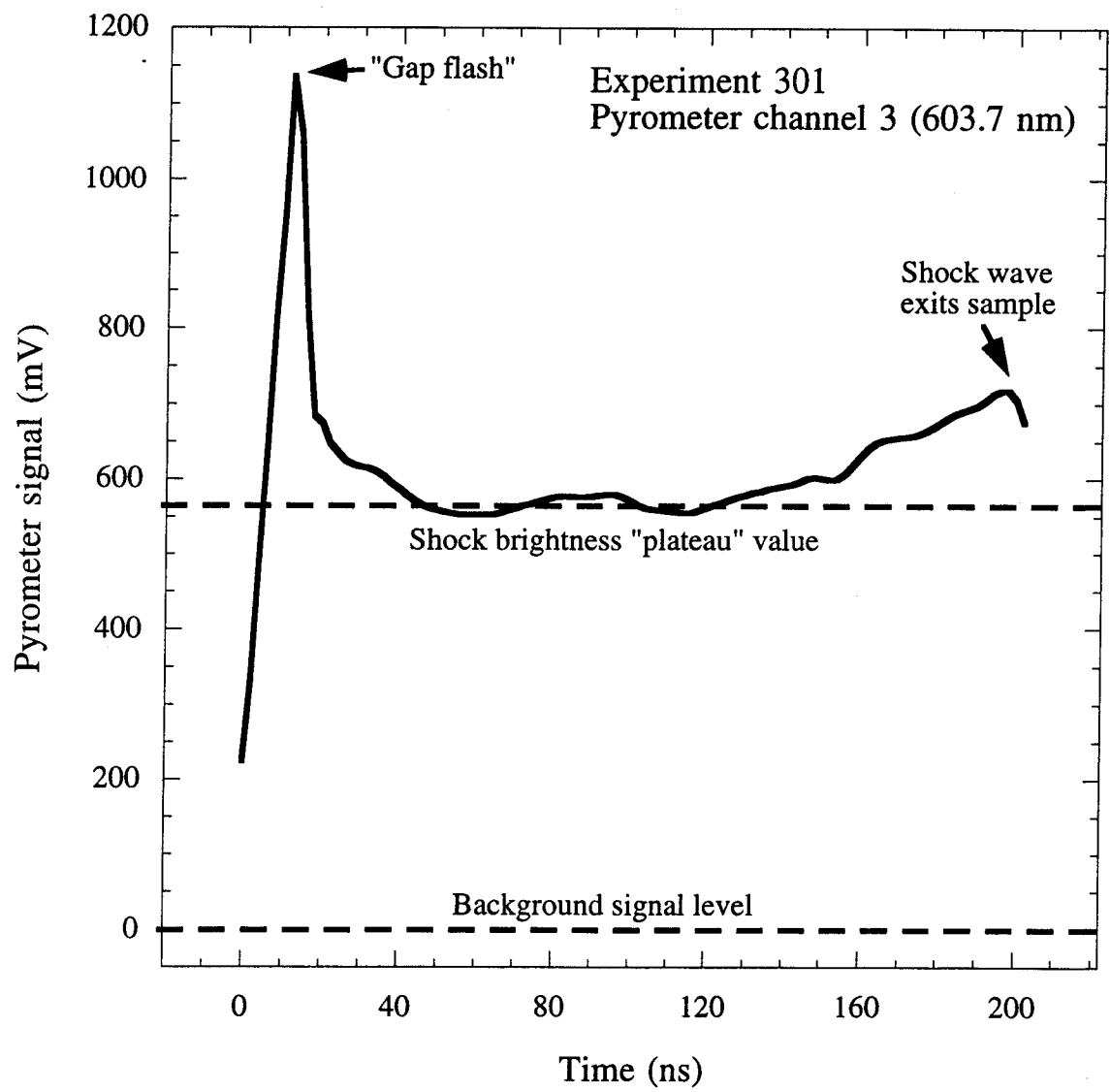


Love and Ahrens, Fig. 1

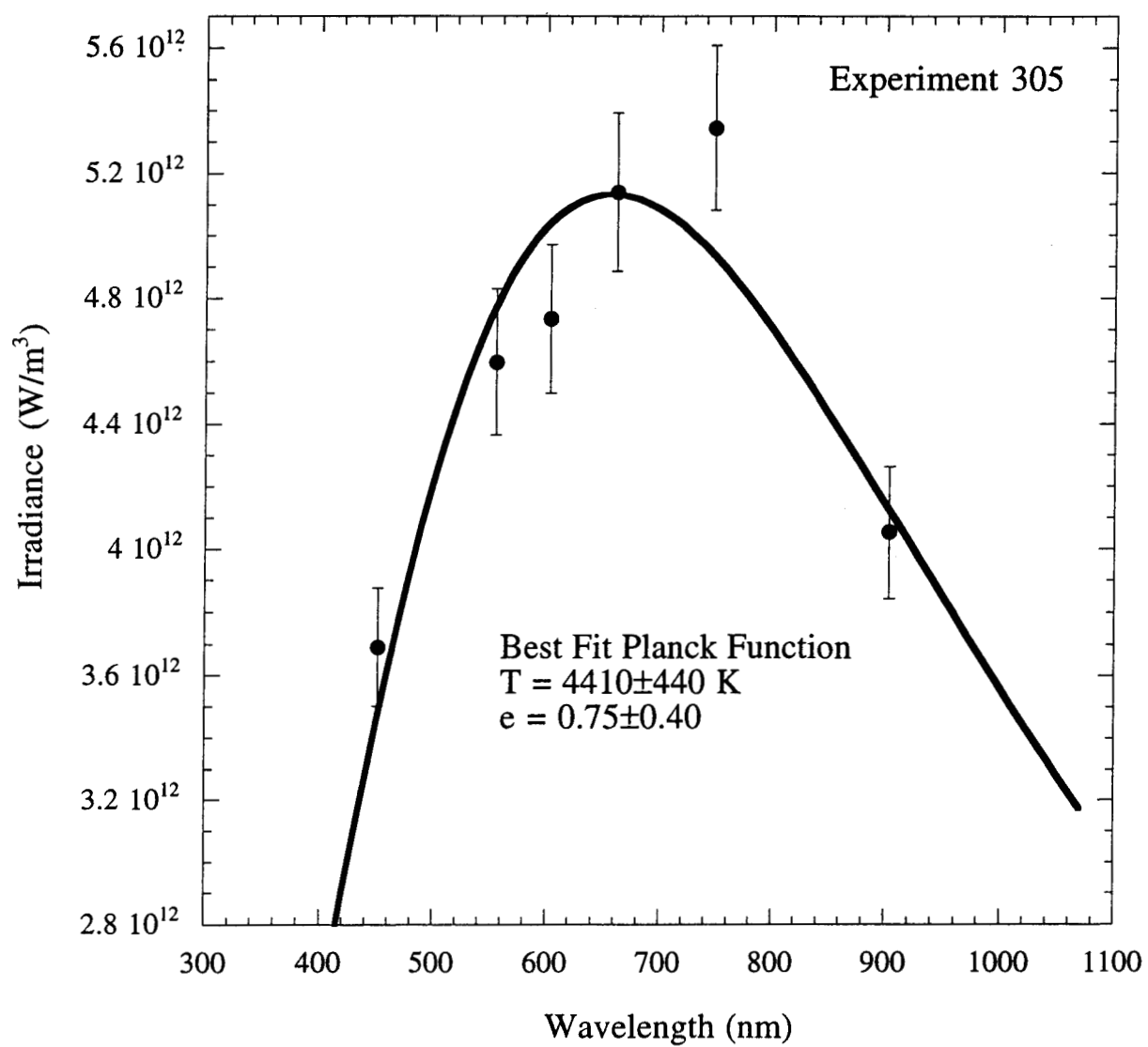


Love and Ahrens, Fig. 2

Love and Ahrens, Fig. 3

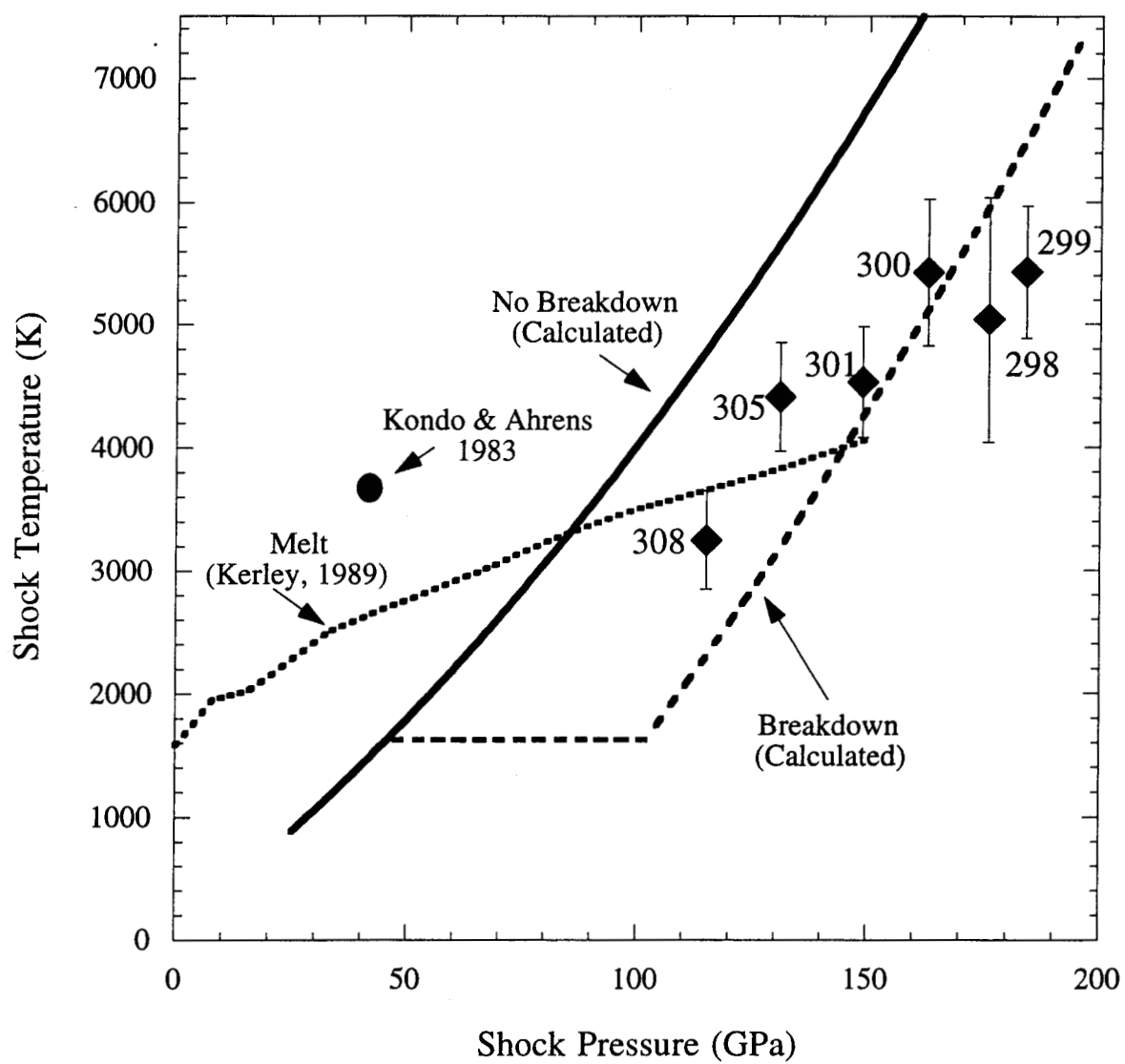


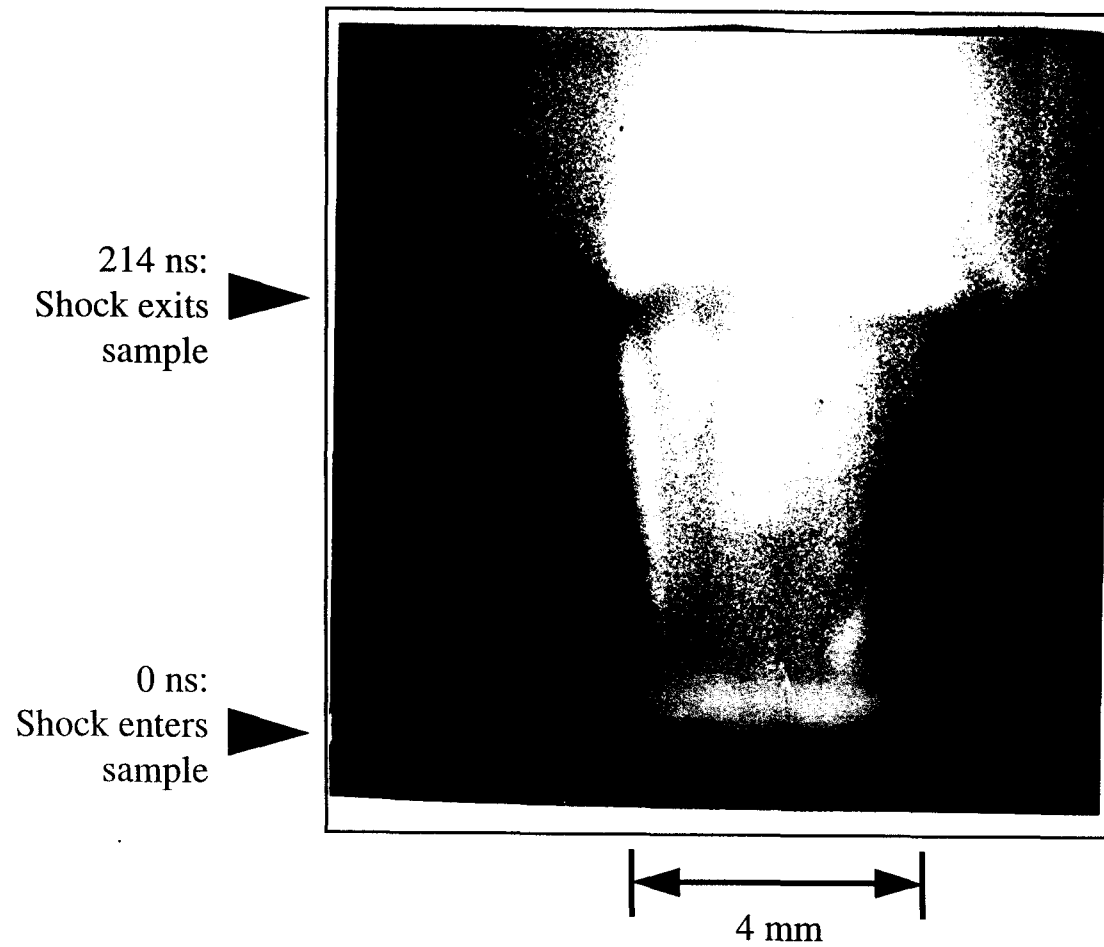
Love and Ahrens, Fig. 4





Love and Ahrens, Fig. 5



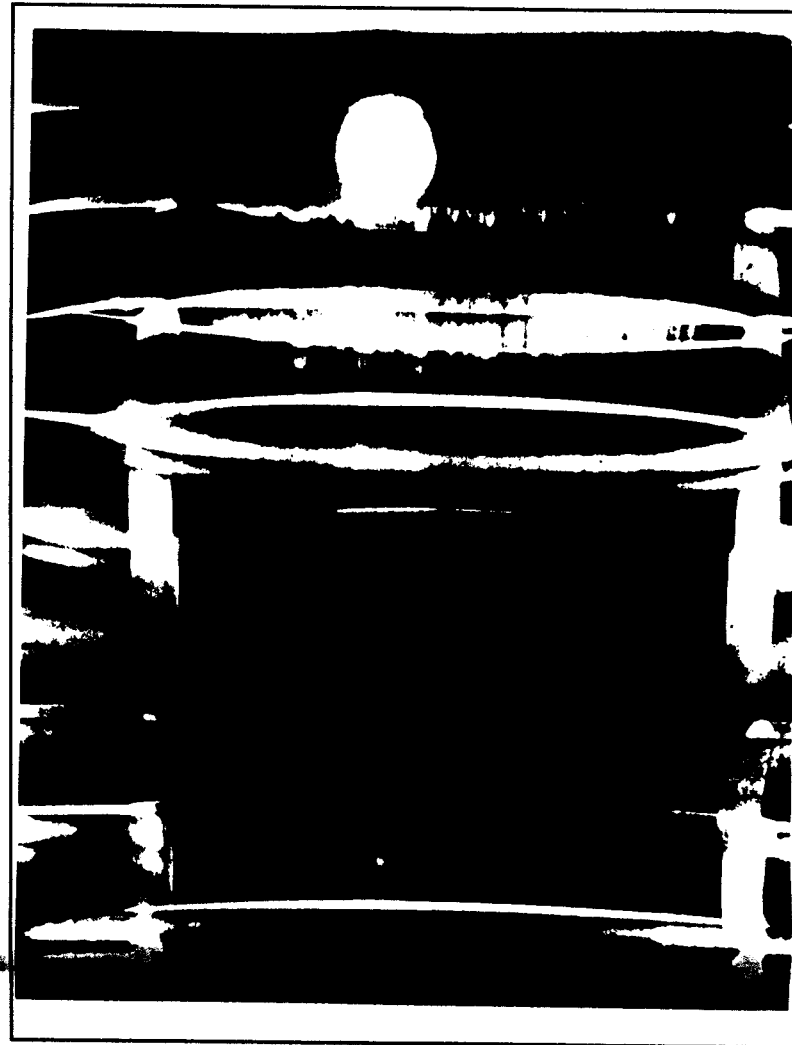


Love and Ahrens, Fig. 6

Image #3

Image #2

Image #1



5 mm

Love and Ahrens, Fig. 7